

Banner appropriate to article type will appear here in typeset article

# A compressible Reynolds-averaged mixing model considering turbulent entropy and heat flux

Hansong Xie<sup>1</sup>, Tengfei Luo<sup>4,5</sup>, Yaomin Zhao<sup>1</sup> †, Yousheng Zhang<sup>1,2,3</sup> ‡ and Jianchun Wang<sup>4</sup>

<sup>1</sup>HEDPS, Center for Applied Physics and Technology, and College of Engineering, Peking University, Beijing 100871, China

<sup>2</sup>Institute of Applied Physics and Computational Mathematics, Beijing 100094, China

<sup>3</sup>National Key Laboratory of Computational Physics, Beijing 100088, China

<sup>4</sup>Department of Mechanics and Aerospace Engineering, Southern University of Science and Technology, Shenzhen 518055, China

<sup>5</sup>Center for Ocean Research in Hong Kong and Macau, and Division of Environment and Sustainability, Hong Kong University of Science and Technology, Hong Kong, China

(Received xx; revised xx; accepted xx)

In typical nature and engineering scenarios, such as supernova explosion and inertial confinement fusion, mixing flows induced by hydrodynamics interfacial instabilities are essentially compressible. Despite their significance, accurate predictive tools for these compressible flows remain scarce. For engineering applications, the Reynolds-averaged Navier-Stokes (RANS) simulation stands out as the most practical approach due to its outstanding computational efficiency. However, the majority of RANS mixing studies reported have concentrated on incompressible scenarios, with quite limited attention given to compressible cases. Moreover, most of the existing RANS mixing models demonstrate significantly inaccurate predictions for compressible mixing flow. This study develops a novel compressible RANS mixing model by incorporating physical compressibility corrections into the incompressible  $K - L - \gamma$  mixing transition model recently proposed by Xie *et al.* (*J. Fluid Mech.*, 1002, A31, 2025). Specifically, taking the density-stratified Rayleigh-Taylor mixing flows as representative compressible cases, we firstly analyze the limitations of the existing model for compressible flows, based on high-fidelity data and local instability criteria. Subsequently, the equation of state for a perfect gas and the thermodynamic Gibbs relation are employed to derive comprehensive compressibility corrections. The crucial turbulent entropy and heat flux are integrated into the closure of the key turbulent mass flux term of the turbulent kinetic energy equation. These corrections enable the model to accurately depict compressible mixing flows. Systematic validations confirm the efficacy of the proposed modeling scheme. This study offers a promising strategy for modeling compressible mixing flows, paving the way for more accurate predictions in complex scenarios.

**Key words:** compressible mixing flows, compressible RANS model, density-stratified RT, mixing transition

† Email address for correspondence: yaomin.zhao@pku.edu.cn

‡ Email address for correspondence: zhang\_yousheng@iapcm.ac.cn

**Abstract must not spill onto p.2**

## 1. Introduction

This investigation focuses on mixing flows induced by hydrodynamic interfacial instabilities, such as the Rayleigh-Taylor (RT) (Rayleigh 1882; Taylor 1950) and Richtmyer-Meshkov (RM) (Richtmyer 1960; Meshkov 1969) instabilities. The RT instability arises when a denser fluid is accelerated by a lighter one under constant acceleration, while the RM instability emerges if the acceleration is pulsing regardless of the shocking direction. In both cases the misalignment between density and pressure gradients drives interfacial perturbation growth. Baroclinic vorticity plays a crucial role in amplifying interfacial perturbations while simultaneously entraining surrounding irrotational fluids into the mixing zone. Mixing is frequently intensified by the Kelvin-Helmholtz instability (Kelvin 1871; Helmholtz 1868), and subsequently transitions to turbulence. This interfacial mixing phenomenon is observed in systems spanning multiple scales, from cosmic-scale supernova explosions to laboratory-scale applications in scramjet propulsion and inertial confinement fusion (ICF) (Zhou 2017a). The prevalence of these mixing processes across such diverse physical systems underscores their fundamental importance in both natural phenomena and engineering applications.

The aforementioned mixing flows essentially demonstrate significant compressibility effects across numerous scenarios. Taking ICF as an example, the internal flow can be characterized as a highly nonlinear compressible system progressing through four characteristic stages: shock-transit, acceleration, deceleration, and peak compression (Craxton *et al.* 2015). The first stage typically initiates with a sequence of laser pulses of increasing intensities irradiating the ICF target. These pulses generate pressure waves in the plasma, launching a sequence of shock waves that propagate into and compress the target. During this stage, surface perturbations on the shells evolve as a result of a RM-like instability, due to imperfections in fabrication and laser-beam nonuniformity. After the shock reaches the inner surface, the acceleration stage begins, characterized by an outward-moving rarefaction wave and inward acceleration of the target shells. The subsequent deceleration stage sees continued shell compression with a gradually decreasing speed through centripetal inertia, with kinetic energy converted into internal energy, resulting in increase of pressure and temperature. The compression process culminates in peak compression phase, where the fuel reaches the maximum compression level, yielding central hot spots with extraordinarily high temperature and density due to compressibility. Throughout these stages, hydrodynamic instabilities, particularly the RT and RM instabilities, amplify surface perturbations, compromising shell integrity and compression efficiency. The resulting mixing flows dissipate substantial energy, cooling the fuel and potentially causing ignition failure. Notably, the density profiles within each shell vary radially as the radial location  $r$ , as illustrated in figure 1(b), contrasting with the constant density profiles of incompressible cases in figure 1(a). This ignition process underscores the critical importance of studying compressible mixing flows.

Current studies on compressible mixing flows primarily focus on those induced by RT instability, where compressibility effects stem from two distinct origins (Gauthier & Le Creurer 2010). The first is the static compressibility, which results from the fluid's variable density. In an acceleration field, it causes density stratification and gradient for light and heavy fluids. The second is dynamic compressibility, an effect fundamentally associated with the finite speed of sound. For a perfect gas, it can be characterized by the adiabatic indices  $\Gamma$  in the equation of state (EOS). The dynamic compressibility mainly depends on the inherent properties of the fluid, while existing numerical and theoretical investigations have demonstrated that compressibility in RT flows is predominantly governed by static

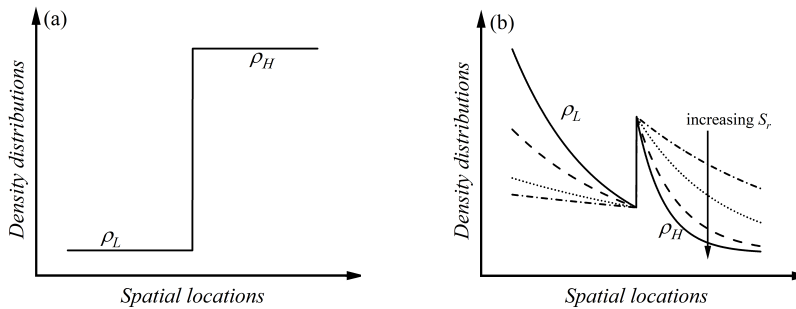


Figure 1: Schematic diagrams of the initial density distributions for (a) the incompressible and (b) the density-stratified compressible RT flows.

compressibility (Livescu 2004; Jin *et al.* 2005; Xue & Ye 2010; Gauthier 2013, 2017). Therefore, the present study concentrates on static compressibility, specifically density-stratified compressible RT mixing flows.

The classical incompressible RT mixing, as illustrated in figure 1(a), maintains initial constant density distributions within both light and heavy fluid layers. In contrast, the density-stratified compressible RT mixing initially displays significant density gradient, as depicted in figure 1(b). Under the isothermal condition, this density distribution exhibits exponential variation with the spatial locations. The stratification strength is commonly quantified using the density stratification parameter (Luo & Wang 2022):

$$S_r \equiv \frac{gL_r}{RT_r/M_r}, \quad (1.1)$$

with  $g$ ,  $L_r$ ,  $T_r$ ,  $M_r$ , and  $R$  representing the gravitational acceleration, characteristic length, temperature, mole mass, and universal gas constant, respectively. The larger  $S_r$  corresponds to a steeper density gradient, indicating a stronger compressibility effect. This fundamental difference highlights the distinctive behavior of compressible versus incompressible RT mixing.

Existing studies have revealed prominent differences between density-stratified compressible RT flows and their incompressible counterparts. Owing to the initial density stratification, the growth rate of RT mixing is substantially affected (Xue & Ye 2010). George & Glimm (2005) have emphasized that self-similar rates differ markedly between compressible and incompressible scenarios, noting that the quadratic growth rate with time (denoted as  $t$ ) observed in incompressible cases cannot be directly applied to compressible flows. This perspective has been corroborated by high-fidelity (HiFi) numerical simulations conducted by Gauthier (2017) and Luo & Wang (2022), which confirm that the  $t^2$ -scaling law does not hold for density-stratified compressible RT mixing flows. Furthermore, density stratification enhances asymmetric evolution of the mixing layers on the light and heavy fluid sides. Additionally, these studies have revealed that spatial profiles of density and temperature are significantly influenced by initial density stratification, exhibiting complex distributions that contrast with the monotonic variations seen in incompressible cases.

Energy transport mechanisms also exhibit fundamental differences between density-stratified compressible and incompressible RT flows. For the compressible cases, kinetic energy generation stems from two primary sources: potential energy conversion and pressure-dilatation work (Zhao *et al.* 2020; Luo & Wang 2022). When the  $S_r$  is small, the kinetic energy derives predominantly from potential energy, which is similar to the incompressible situation. However, for larger  $S_r$ , pressure-dilatation work becomes the dominant mechanism

for kinetic energy generation. Moreover, the kinetic energy is subsequently converted back into potential energy. These observations demonstrate that the underlying energy transport physics differs substantially between compressible and incompressible RT flows (Zhao *et al.* 2022).

While considerable progress has been made in understanding the fundamental mechanisms of density-stratified compressible RT flows, modeling efforts remain limited. Current researches primarily focus on two approaches: the buoyancy-drag model (Jin *et al.* 2005; Fu *et al.* 2022) and the large-eddy simulation (LES) techniques (Luo *et al.* 2024). However, significant limitations persist. The buoyancy-drag model, while computationally efficient, oversimplifies the physics and fails to capture essential flow characteristics required for engineering applications. Conversely, LES provides more detailed flow information but at prohibitively high computational costs, making it impractical for routine engineering predictions. This disparity underscores the urgent need to develop alternative modeling approaches that can provide acceptable computational accuracy at an affordable cost, which is a critical step toward practical engineering applications of compressible RT flow predictions.

Reynolds-averaged Navier-Stokes (RANS) simulation has been widely adopted in industrial applications owing to its favorable balance between computational efficiency and cost. A number of RANS mixing models have been proposed for interfacial flow predictions, such as the  $K - L$  (Dimonte & Tipton 2006; Morgan & Greenough 2015; Kokkinakis *et al.* 2019; Zhang *et al.* 2020),  $K - \epsilon$  (Morán-López & Schilling 2013; Xie *et al.* 2021a), and BHR models (Denissen *et al.* 2014; Xie *et al.* 2021b). However, most of the existing RANS models predominantly address incompressible flows. The fundamental differences between compressible and incompressible RT mixing flows, as previously discussed, render existing RANS models inadequate for compressible scenarios. Indeed, compressible RANS modeling remains largely unexplored — a critical gap this study seeks to address. Our approach builds upon the recently proposed  $K - L - \gamma$  mixing transition model (Xie *et al.* 2025), which has been shown to have good performance for capturing the mixing transition process in incompressible flows. Through systematic compressibility modifications, we extend this model to accurately capture both the transition dynamics (Qi *et al.* 2024) and compressibility effects in compressible mixing flows.

This paper is organized as follows. Section 2.1 presents the governing equations of the baseline  $K - L - \gamma$  mixing transition model. The performance of this baseline model for density-stratified compressible RT flows is then evaluated in section 2.2. Through comparison with HiFi simulation data and application of local instability criteria, the fundamental limitations of the baseline model applied to compressible RT flows are systematically analyzed. Section 2.3 details the theoretical derivation of the proposed compressibility modifications. These developments are subsequently validated in section 3, where computational results demonstrate the improved predictive capability. Finally, section 4 presents discussions and summarizes the contributions of the present study.

## 2. Methodology

### 2.1. Governing equations and baseline model

For mixing flows, the multicomponent RANS equations are solved considering molecular transport and thermodynamic coefficients. The transport equations for the mean density  $\bar{\rho}$ , velocity  $\bar{u}_i$ , total energy  $\bar{E}$  of the mixture, and mass fraction  $\bar{Y}_\alpha$  of species  $\alpha$  are given as

follows:

$$\frac{\partial \bar{\rho}}{\partial t} + \frac{\partial \bar{\rho} \tilde{u}_j}{\partial x_j} = 0, \quad (2.1)$$

$$\frac{\partial \bar{\rho} \tilde{u}_i}{\partial t} + \frac{\partial \bar{\rho} \tilde{u}_i \tilde{u}_j}{\partial x_j} + \frac{\partial \bar{p}}{\partial x_i} - \bar{\rho} g_i = -\frac{\partial \tau_{ij}}{\partial x_j} + \frac{\partial \bar{\sigma}_{ij}}{\partial x_j}, \quad (2.2)$$

$$\frac{\partial \bar{\rho} \tilde{E}}{\partial t} + \frac{\partial (\bar{\rho} \tilde{E} + \bar{p}) \tilde{u}_j}{\partial x_j} - \bar{\rho} \tilde{u}_i g_i = D_E + D_K + \frac{\partial}{\partial x_j} (-\tau_{ij} \tilde{u}_i + \bar{\sigma}_{ij} \tilde{u}_i - \bar{q}_c - \bar{q}_d), \quad (2.3)$$

$$\frac{\partial \bar{\rho} \tilde{Y}_\alpha}{\partial t} + \frac{\partial \bar{\rho} \tilde{Y}_\alpha \tilde{u}_j}{\partial x_j} = D_Y + \frac{\partial}{\partial x_j} \left( \bar{\rho} \tilde{D} \frac{\partial \tilde{Y}_\alpha}{\partial x_j} \right). \quad (2.4)$$

The overbar and tilde represent the Reynolds and Favre averaged fields, respectively. The subscripts  $i, j = 1, 2, 3$  denote three spatial directions ( $x, y, z$ ). The  $\bar{p}$  denotes pressure of the mean field. The heat flux  $\bar{q}_c$ , the interspecies diffusional heat flux  $\bar{q}_d$ , and the viscous stress tensor  $\bar{\sigma}_{ij}$  are given as  $\bar{q}_c = -\bar{\kappa} \partial \bar{T} / \partial x_j$ ,  $\bar{q}_d = -\sum \bar{\rho} \tilde{D} \bar{c}_{p,\alpha} \tilde{\partial Y}_\alpha / \partial x_j$ ,  $\bar{\sigma}_{ij} = 2\bar{\mu} (\tilde{S}_{ij} - \tilde{S}_{kk} \delta_{ij} / 3)$ ,  $\tilde{S}_{ij} = (\partial \tilde{u}_i / \partial x_j + \partial \tilde{u}_j / \partial x_i) / 2$ . Here  $\bar{\mu}$ ,  $\tilde{D}$ ,  $\bar{\kappa}$ , and  $\bar{c}_{p,\alpha}$  represent dynamic viscosity, mass diffusivity, thermal conductivity, and constant-pressure specific heat of species  $\alpha$ , respectively. In correspondence with Livescu (2013), the mixture's EOS  $\bar{p} \tilde{M} = \bar{\rho} R \tilde{T}$  is used, which is calculated with the assumptions of iso-temperature (i.e.  $T_1 = T_2 = \dots = T_\alpha$ ) and partial-pressure (i.e.  $p = \sum p_\alpha$ ), and the fluid properties of the mixture are determined using the species-linearly weighted assumption.

Equations (2.1)~(2.4) are deduced based on the ensemble average operation, which results in the unclosed terms, i.e. the Reynolds stress  $\tau_{ij}$ , the turbulent diffusion terms  $D_E$ ,  $D_K$  and  $D_Y$  of the total energy, the turbulent kinetic energy (TKE,  $\tilde{K}$ ), and the mass fraction, respectively. With the widely used gradient diffusion assumption (GDA), that the turbulent flux of an arbitrary physical variable  $f$  can be proportional to its mean gradient, i.e.

$$-\overline{\bar{\rho} u_j'' f''} = \frac{\mu_t}{N_f} \frac{\partial \tilde{f}}{\partial x_j} \quad \text{or} \quad -\overline{\bar{\rho} u_j' f'} = \frac{\mu_t}{N_f} \frac{\partial \tilde{f}}{\partial x_j}, \quad (2.5)$$

where “''” and “'” denote the Reynolds and Favre fluctuations respectively, as well as  $N_f$  being a model coefficient, these turbulent diffusion terms are modeled as  $D_E = \frac{\partial}{\partial x_j} \left( \frac{\mu_t}{N_h} \frac{\partial \tilde{h}}{\partial x_j} \right)$ ,  $D_K = \frac{\partial}{\partial x_j} \left( \frac{\mu_t}{N_K} \frac{\partial \tilde{K}}{\partial x_j} \right)$ ,  $D_Y = \frac{\partial}{\partial x_j} \left( \frac{\mu_t}{N_Y} \frac{\partial \tilde{Y}}{\partial x_j} \right)$ , respectively, the enthalpy  $h = e + p/\rho = c_p T$ ,  $e$  representing internal energy.

In the  $K - L - \gamma$  model, the TKE  $\tilde{K}$  and the turbulent length scale  $\tilde{L}$  are used to describe the turbulent viscosity  $\nu_t$ , which is limited by the intermittent factor  $\gamma$  to enable this model to describe mixing transition flows (Xie *et al.* 2025). The  $\mu_t$  is expressed as  $\mu_t = \bar{\rho} \nu_t = C_\mu \bar{\rho} \gamma \tilde{L} \sqrt{2\tilde{K}}$ , where  $C_\mu$  is a model coefficient. Based on the classical Boussinesq eddy viscosity hypothesis, the Reynolds stress is modeled as  $\tau_{ij} = C_P \bar{\rho} \tilde{K} \delta_{ij} - 2\mu_t (\tilde{S}_{ij} - \tilde{S}_{kk} \delta_{ij} / 3)$ , here  $C_P$  is a model coefficient and  $\delta_{ij}$  is the Kronecker symbol. To describe the spatio-

temporal evolutions of the  $\tilde{K}$ ,  $\tilde{L}$  and  $\gamma$ , their transport equations are introduced as follows:

$$\frac{\partial \bar{\rho} \tilde{K}}{\partial t} + \frac{\partial \bar{\rho} \tilde{K} \tilde{u}_j}{\partial x_j} = -\tau_{ij} \frac{\partial \tilde{u}_i}{\partial x_j} + \frac{\partial}{\partial x_j} \left( \frac{\mu_t}{N_K} \frac{\partial \tilde{K}}{\partial x_j} \right) + S_{Kf} - C_D \bar{\rho} (\sqrt{2\tilde{K}})^3 / \tilde{L}, \quad (2.6)$$

$$\frac{\partial \bar{\rho} \tilde{L}}{\partial t} + \frac{\partial \bar{\rho} \tilde{L} \tilde{u}_j}{\partial x_j} = \frac{\partial}{\partial x_j} \left( \frac{\mu_t}{N_L} \frac{\partial \tilde{L}}{\partial x_j} \right) + C_L \bar{\rho} \sqrt{2\tilde{K}} + C_C \bar{\rho} \tilde{L} \frac{\partial \tilde{u}_j}{\partial x_j}, \quad (2.7)$$

$$\frac{\partial \bar{\rho} \gamma}{\partial t} + \frac{\partial \bar{\rho} \gamma \tilde{u}_j}{\partial x_j} = \frac{\partial}{\partial x_j} \left( \frac{\mu_t}{N_\gamma} \frac{\partial \gamma}{\partial x_j} \right) + P_\gamma - \epsilon. \quad (2.8)$$

The  $P_\gamma = F_{onset} G_r$  is the production term of the  $\gamma$  equation, the dissipation term  $\epsilon = \gamma P_\gamma$  ensuring the intermittent factor varying from 0 to 1. The  $F_{onset}$  serves as a transition switch, and  $G_r$  describes the growth of  $\gamma$ , which are expressed as

$$F_{onset} = 1 - \frac{1}{e^{\max(0, Re_t - Re_{tra})}}, \quad Re_t = \frac{\tilde{L} \sqrt{\tilde{K}}}{\nu}, \quad (2.9)$$

$$G_r = C_1 \sqrt{\gamma} \left\{ (1 - \gamma) \left[ \bar{\rho} \sqrt{2\tilde{S}_{ij}\tilde{S}_{ij}} + C_2 \sqrt{\max\left(0, -\frac{\partial \bar{\rho}}{\partial x_k} \frac{\partial \bar{\rho}}{\partial x_k}\right)} \right] + \left( \gamma S_{Kf} - \tau_{ij} \frac{\partial \tilde{u}_i}{\partial x_j} \right) / \tilde{K} \right\}. \quad (2.10)$$

Here,  $C_1$  and  $C_2$  are model coefficients,  $\nu$  denoting the kinetic viscosity, and  $Re_{tra}$  denoting a pre-defined key transition Reynolds number set to 10, following Xie *et al.* (2025).

The buoyancy-driven source term  $S_{Kf}$  is modeled based on the following advanced formation (Xiao *et al.* 2020),

$$S_{Kf} = \begin{cases} -C_B \frac{\partial \bar{\rho}}{\partial x_i} \sqrt{2\tilde{K}} |(1 - \omega_l) A_{0i} + \omega_l A_{ssi}|, & \text{if } \Theta_{gf} < \Theta_{gm}, \\ -C_B \frac{\partial \bar{\rho}}{\partial x_i} \sqrt{2\tilde{K}} \max[0, (1 - \omega_l) A_{0i} + \omega_l A_{ssi}], & \text{otherwise,} \end{cases} \quad (2.11)$$

where  $C_B$  is a model coefficient. The mean- and turbulent- field accelerations  $\Theta_{gm}$  and  $\Theta_{gf}$  are used to identify RM and RT mixings, whose expressions can be seen in Xiao *et al.* (2020). The initial cell Atwood number  $A_{0i}$  describes the density's discontinuous characteristic at the interfaces between fluids, and can be expressed by the reconstructed values of the densities at the cell's faces (Kokkinakis *et al.* 2015). The local Atwood number  $A_{ssi}$  in the self-similar regime depicts the density's gradual variation, and is calculated by

$$A_{ssi} = \frac{C_A \tilde{L}}{\bar{\rho} + \tilde{L}} \frac{\partial \bar{\rho}}{\partial x_i}, \quad (2.12)$$

where  $C_A$  is a model coefficient. The weighting factor  $\omega_l = \min(\frac{\tilde{L}}{\Delta x}, 1)$  ( $\Delta x$  is the grid scale) ensures that mixing evolution is solely decided by  $A_{ssi}$  when  $\tilde{L}$  becomes sufficiently large, while initially is dominated by  $A_{0i}$  (Kokkinakis *et al.* 2015).

Equations (2.1)~(2.4), (2.6)~(2.12) constitute the complete  $K - L - \gamma$  mixing transition model, which has demonstrated a good capability for predicting incompressible RT/RM mixing transition flows. More details about this model can be found in Xie *et al.* (2025). Given the prominent transition processes observed in density-stratified compressible RT mixing flows, the  $K - L - \gamma$  model is adopted as the baseline model in this study to be expected to capture the transition effect. In the next section, performance of the baseline model for the targeted flows will be evaluated. In addition, the widely used  $K - L$  model, which is designed for fully developed turbulent mixing flows, is also tested for comparison, highlighting the necessity of considering the transitional effects by introducing the  $\gamma$  equation.

## 2.2. Baseline model evaluation for compressibility effects

The evaluated cases originate from the three-dimensional (3D) simulation of initially isothermal density-stratified compressible RT mixing implemented by Luo & Wang (2022). These simulations solved the multicomponent Navier-Stokes equations for cases with different density stratification parameters  $S_r = 0.5, 1, 2$  and  $3$ . An eighth-order central compact finite difference scheme were employed on a uniform grid of  $1024 \times 512 \times 512$  grid points in a rectangular box  $x \times y \times z$  of  $2L_r \times L_r \times L_r$ ,  $L_r = 1$ . Time integration is performed using a third-order Runge-Kutta scheme. The simulations of Luo & Wang (2022) are thus highly resolved and referred to as HiFi simulations in the present study.

Due to homogeneity of the flow in the spanwise plane (i.e. the  $y - z$  plane), the 3D cases are statistically reduced to the one-dimensional (1D) equivalents for RANS computations. The flow configuration is described as follows. The light and heavy fluids, represented by the subscript  $L$  and  $H$  respectively, are initially placed in the computational domains  $[-L_x, 0]cm$  and  $[0, L_x]cm$  respectively, with  $L_x = L_r = 1$ . A constant gravitational acceleration  $g = 1cms^{-2}$  is imposed along the  $-x$  direction. Both fluids are compressible ideal gases with the same adiabatic exponent  $\Gamma = 5/3$ , and the molar mass  $M_L$  and  $M_H$  are  $0.029kg/mol$  and  $0.087kg/mol$ , respectively, yielding an Atwood number  $A_t \equiv \frac{M_H - M_L}{M_H + M_L} = 0.5$ , consistent with the definition in Luo & Wang (2022). The stratification parameter  $S_r$  is defined based on the formula (1.1). The characteristic Reynolds number  $Re \equiv \frac{g^{1/2}L_r^{3/2}}{\mu_r/\rho_r} = 10000$ , the Prandtl number and the Schmidt number are  $0.7$  and  $1.0$ , respectively. Reference quantities used to define these dimensionless parameter include the temperature  $T_r = T_H = T_L$ , molar mass  $M_r = (M_H + M_L)/2$ , dynamic viscosity  $\mu_r = \mu_H = \mu_L$ , density  $\rho_r = (\rho_{H,0} + \rho_{L,0})/2$ , where  $\rho_{H,0}$  and  $\rho_{L,0}$  represent the initial densities on either side of the interface. Additionally, the characteristic time scale is defined as  $\tau = \sqrt{L_r/(A_t g)}$ . All reference quantities are consistent with the HiFi simulations to ensure direct comparability between RANS and HiFi results. The system is initialized with a hydrostatic background state in thermal equilibrium. By setting  $\tilde{u} = 0$  in the momentum equation, we can obtain the initial density and pressure distributions:

$$p_m = p_I \exp\left(-\frac{gx}{(R/M_m)T_I}\right), \quad (2.13)$$

$$\rho_m = \frac{p_I}{(R/M_m)T_I} \exp\left(-\frac{gx}{(R/M_m)T_I}\right), \quad (2.14)$$

where  $p_I$  and  $T_I$  represent the initial pressure and temperature at the interface, respectively, the subscript  $m$  representing either heavy ( $H$ ) or light ( $L$ ) fluid. Specifically,  $p_I = 1gcm^{-1}s^{-2}$ ,  $T_I$  equals to  $T_r$  determined based on the formula (1.1). Figure 2 shows comparisons of the initial density and pressure fields from RANS and HiFi simulations, ensuring the correctness of the present configurations.

Performance of the baseline model for the targeted flows is tested here. The RANS calculations are implemented in the finite difference code for compressible fluid dynamics developed by Y. Zhang *et al.* since 2016, which has been extensively validated for RT and RM mixing studies (Xie *et al.* 2025; Zhang *et al.* 2020; Xiao *et al.* 2025; Li *et al.* 2019; Xiao *et al.* 2022; Xie *et al.* 2023). A combination of MUSCL5, i.e. the improved total variation diminishing scheme with a fifth-order limiter, and the Riemann solver proposed by Toro *et al.* (1994) is used to calculate the convection terms. To reduce the numerical dissipation, low Mach number modification (Thorner *et al.* 2008a,b) is used during the reconstruction of the half-point flux. The diffusion terms are calculated with the sixth-order central difference

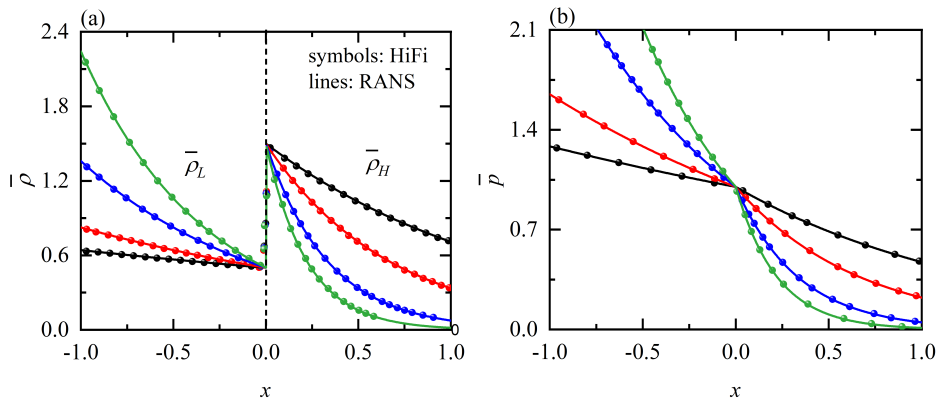


Figure 2: Initial distributions for density and pressure fields. The symbols and lines represent the initial flow fields of HiFi simulations and RANS simulations, respectively. The lines colored by black, red, blue, and green correspond to cases of  $S_T = 0.5, 1, 2$  and  $3$ , respectively.

Table 1: Model coefficients of the baseline model.

$C_C$	$C_P$	$C_L$	$N_K$	$N_L$	$N_\gamma$	$N_Y$	$N_h$	$C_\mu$	$C_B$	$C_A$	$C_D$	$C_1$	$C_2$
1/3	2/3	0.189	1.069	0.096	0.100	0.869	0.869	1.186	0.482	7.088	0.200	2.200	0.015

scheme. The temporal integration marches with a third-order Runge–Kutta scheme, with Courant–Friedrichs–Lewy number 0.05.

The model coefficients used in the baseline model are listed in table 1, which are determined based on the methodology proposed by Zhang *et al.* (2020). For initialization of the turbulence model variables, we adopt the common practices: nearby the interface the initial turbulent length scale  $\tilde{L}_0$  is  $0.04\text{cm}$ , approximating to the corresponding 3D simulation’s initial perturbation width, the initial TKE  $\tilde{K}_0$  is  $0.0001A_t g \tilde{L}_0 (\text{cm/s})^2$ , as well as the initial intermittent factor  $\gamma_0 = 1 \times 10^{-16}$  following Xie *et al.* (2025).

Figure 3 presents temporal evolution of the mixing width, an important statistical quantity used to characterize the global evolution of mixing flows. The mixing width is defined as:

$$W_b = 3 \int_0^{L_x} \bar{X}(1 - \bar{X})dx, \quad W_s = 3 \int_{-L_x}^0 \bar{X}(1 - \bar{X})dx. \quad (2.15)$$

The mole fraction  $X$  is calculated by the mass fraction (Luo & Wang 2022). The  $W_b$  and  $W_s$  represent the bubble mixing width, i.e. distance of the light fluid penetrating the heavy fluid, and the spike mixing width, i.e. distance of the heavy fluid penetrating the light fluid, respectively. Figure 3(a) shows the prediction results of the  $K - L$  model, which gives a  $t^2$ -scaling law throughout the entire simulation for all cases, failing to depict the transition process. This is expected because the  $K - L$  model is only suitable for the incompressible fully developed turbulent mixing flows. In contrast, the baseline model performs well during the instability development and mixing transition stages at approximately  $(t/\tau)^2 < 4$ , providing predictions consistent with HiFi data for all cases, as illustrated in figure 3(b). It is attributed to that the baseline model can capture mixing transition processes effectively. Beyond the transition stage, the mixing width predicted by the baseline model exhibits a quadratic growth

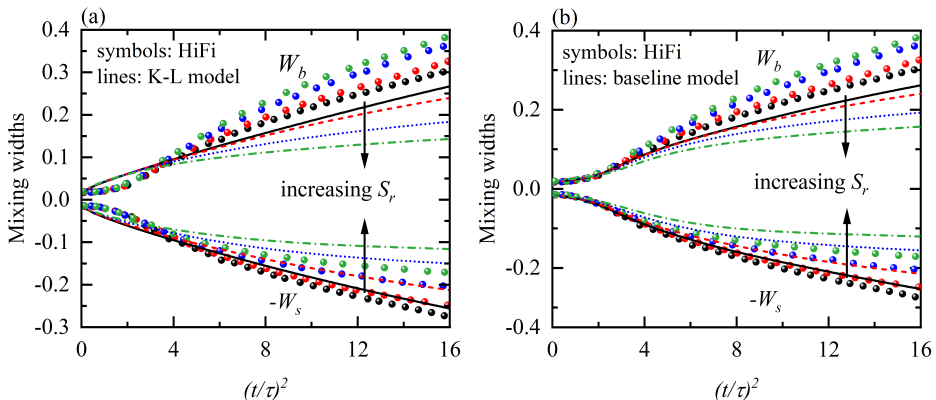


Figure 3: Temporal evolution of the mixing width predicted by (a) the  $K-L$  model and (b) the  $K-L-\gamma$  baseline model. The colors used to distinct different  $S_r$  cases are consistent with figure 2.

in time, according with the late-stage self-similar evolution of incompressible RT mixing flows. Figure 3 highlights the superior capability of the baseline model in predicting mixing transition flows.

Notably, during the early stage, the baseline model gives consistent predictions with HiFi simulations across all compressibility strengths considered here, even though it is essentially an incompressible model. It is attributed to the negligible compressibility effects in early development of the density-stratified RT mixing flows, where behavior closely resembles incompressible cases (Gauthier 2017). However, the baseline model's performance deteriorates significantly during intermediate and late stages. The discrepancies between RANS predictions and HiFi data progressively widen with increasing  $S_r$  values. It can be understood as follows. The  $S_r$  directly correlates with the compressibility strength: a smaller  $S_r$  corresponds to a weaker compressibility effect, flow approaching to the incompressible case as  $S_r \rightarrow 0$ . In the case of  $S_r = 0.5$ , the compressibility is not prominent so that the baseline model can give a comparatively reasonable prediction. For the cases with larger  $S_r$ , strong density stratification brings strong compressibility effect, resulting in failures of the baseline model. The degradation in predictive accuracy directly correlates with the strength of density stratification, highlighting the need for compressibility corrections in the existing RANS modeling.

The baseline model consistently underestimates the evolution of mixing width across all cases examined here. To understand the discrepancy, the underlying modeling philosophy is carefully analyzed. For the  $K-L-\gamma$  and the  $K-L$  models, the TKE transport equation plays a crucial role in governing the dynamic evolution of both mixing and turbulence. Following Chassaing *et al.* (2002) and Gauthier (2017), the exact averaged TKE equation without any modeling is written as:

$$\frac{\partial(\bar{\rho}\bar{K})}{\partial t} + \frac{\partial(\bar{\rho}\bar{K}\bar{u}_j)}{\partial x_j} = \underbrace{-\overline{\rho u_i'' u_j''} \frac{\partial \bar{u}_i}{\partial x_j}}_I - \underbrace{\overline{u_i''} \frac{\partial \bar{p}}{\partial x_i}}_II - \underbrace{\frac{\partial(\overline{\rho u_j'' K} + \overline{p' u_j''} + \overline{\sigma_{ij} u_i''})}{\partial x_j}}_III + \underbrace{\overline{p' \frac{\partial u_i''}{\partial x_i}}}_IV - \underbrace{\overline{\sigma_{ij} \frac{\partial u_i''}{\partial x_j}}}_V, \quad (2.16)$$

where terms  $I \sim V$  represent shear production, turbulent mass flux (buoyancy production), diffusion, pressure-strain correlation, and dissipation, respectively. Based on the HiFi

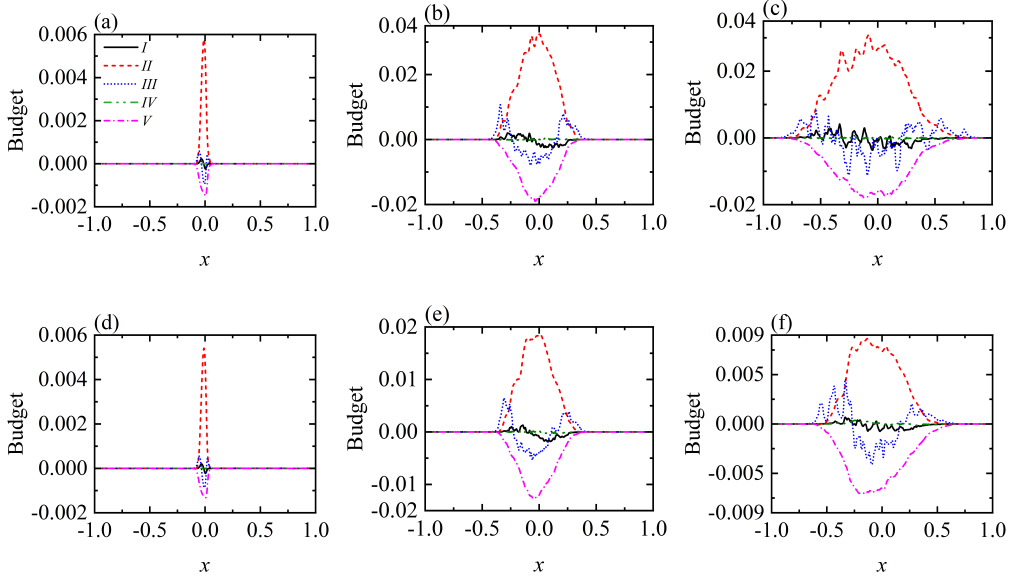


Figure 4: Budgets for terms  $I \sim V$  of the TKE equation (2.16). Subfigures (a)~(c) and (d)~(f) correspond to moments of  $t/\tau = 1, 2.5$  and 4 for cases of  $S_r = 0.5$  and 3 respectively.

simulations, budgets of the terms  $I \sim V$  at  $t/\tau = 1, 2.5$ , and 4 are given in figure 4, where the cases of  $S_r = 0.5$  and 3 are chosen to represent the weak and strong density stratification cases. Figure 4 reveals that the important terms in right hand side of the TKE equation (2.16) are the turbulent mass flux (term  $II$ ) and dissipation (term  $V$ ) terms. Given the dissipation enslaved by the production, the turbulent mass flux  $-\overline{u_i'' \frac{\partial \bar{p}}{\partial x_i}}$  is thus considered as the dominant term.

In the  $K - L - \gamma$  model, the turbulent mass flux  $-\overline{u_i'' \frac{\partial \bar{p}}{\partial x_i}}$  is closed using the term  $S_{Kf}$ , as expressed by the combination of (2.11) and (2.12). Therefore, it is natural to analyze the modeling mechanism of the formulas (2.11) and (2.12), to explore underlying reasons. The key physical mechanism incorporated in  $S_{Kf}$  is the baroclinic term  $\frac{\partial \bar{p}}{\partial x_i} \frac{\partial \bar{p}}{\partial x_i}$ , which acts as an effective production source when  $\frac{\partial \bar{p}}{\partial x_i} \frac{\partial \bar{p}}{\partial x_i} < 0$ ; otherwise  $S_{Kf} = 0$ . The latter condition leads to a stagnation of mixing evolution, consistent with the observations in figure 3, where the growth rate of the mixing width approaches zero for cases with  $S_r = 2$  and 3 during late-stage development. This behavior can be attributed to the premature disappearance of the baroclinic term in the present flows. Specifically, due to the initial density stratification, the sign of the density gradient  $\frac{\partial \bar{p}}{\partial x_i}$  transitions from positive to negative too early in the mixing region. Since the pressure gradient  $\frac{\partial \bar{p}}{\partial x_i}$  remains negative under gravitational field, the product  $\frac{\partial \bar{p}}{\partial x_i} \frac{\partial \bar{p}}{\partial x_i}$  becomes positive once  $\frac{\partial \bar{p}}{\partial x_i} < 0$ , forcing  $S_{Kf} = 0$ . Consequently, the baseline model fails to supply the necessary source term to sustain mixing and turbulence evolution, thereby deviating from the true physical behavior.

Furthermore, stability analysis can serve as a practical tool for investigating compressible stratified flows characterized by finite density gradients and continuous profiles (Gauthier & Le Creurer 2010). Notably, local instability criteria can effectively identify unstable flow regions. For incompressible flow, the necessary and sufficient condition of a stratified

heterogeneous fluid being stable is  $\frac{\partial \rho}{\partial x_i} < 0$  everywhere, whereas for any region where  $\frac{\partial \rho}{\partial x_i} > 0$  the stratification is considered unstable (Chandrasekhar 1961). In gravitational field, the instability condition is expressed as

$$-\frac{\partial \rho}{\partial x_i} \frac{\partial p}{\partial x_i} > 0. \quad (2.17)$$

For compressible flow, the instability criterion within the linear approximation for the Euler equations is suggested as (Gamalii *et al.* 1980):

$$-\frac{\partial p}{\partial x_i} \left( \frac{\partial \rho}{\partial x_i} - \frac{1}{c^2} \frac{\partial p}{\partial x_i} \right) > 0, \quad (2.18)$$

where  $c$  is the isentropic speed of sound. Obviously, the compressible criterion (2.18) can restore to the incompressible one (2.17) as  $c \rightarrow \infty$ .

We further assess the differences of these criteria in identifying unstable regions by analyzing their spatial distributions along the gravitational direction. These distributions are obtained through spanwise-plane average of the HiFi data. Figure 5 reveals that for the case of  $S_r = 0.5$ , both criteria identify identical unstable regions at  $t/\tau = 1$  and 2.5. However, at  $t/\tau = 4$ , the compressible criterion predicts a significantly wider unstable area than its incompressible counterpart, reflecting the baseline model's under-prediction for late-stage mixing evolution. For the case of  $S_r = 3$ , both criteria initially agree at  $t/\tau = 1$  due to negligible compressibility effects in early stages. However, remarkable differences emerge at  $t/\tau = 2.5$  and 4, where the compressible criterion identifies substantially wider unstable regions. These observations thus indicate that the incompressible criterion fails to correctly identify instability when the compressibility effects are significant. Considering that the instability criterion is essential for RANS models as shown in the closures (2.11) and (2.12), the preceding analysis suggests that compressibility effects must be incorporated in modeling the turbulent mass flux.

### 2.3. Compressibility corrections

Analysis of the TKE equation budgets from HiFi simulations confirms that the turbulent mass flux plays a dominant role. Since the seminal work of Dimonte & Tipton (2006), this term  $-\overline{u_i''} \frac{\partial \bar{p}}{\partial x_i}$  has been modeled based on a simple buoyancy-drag model and has received subsequent refinements continuously, leading to the current form (2.11) or similar variants (Kokkinakis *et al.* 2019, 2020). However, compressibility effect has not been considered yet. Indeed, the majority of published RANS mixing studies concentrate on incompressible flows, with quite limited attention given to compressible cases. This section aims to explore how to incorporate compressibility effects into the modeling of the turbulent mass flux term  $-\overline{u_i''} \frac{\partial \bar{p}}{\partial x_i}$ , with a particular focus on the turbulent mass flux velocity  $\overline{u_i''}$ , which serves as a critical component. Utilizing the definitions of Reynolds and Favre averaging, the turbulent mass flux velocity  $\overline{u_i''}$  can be expressed as  $-\frac{\overline{\rho' u_i'}}{\bar{\rho}}$ . This expression highlights that  $\overline{u_i''}$  fundamentally characterizes the turbulent transport on density fluctuations. Therefore, it is natural to explore the potential influence factors on density fluctuation in compressible flows.

To establish a generalized physical relationship, the EOS for a perfect gas is employed in the following form for the mixture:

$$p = (\Gamma - 1)\rho e. \quad (2.19)$$

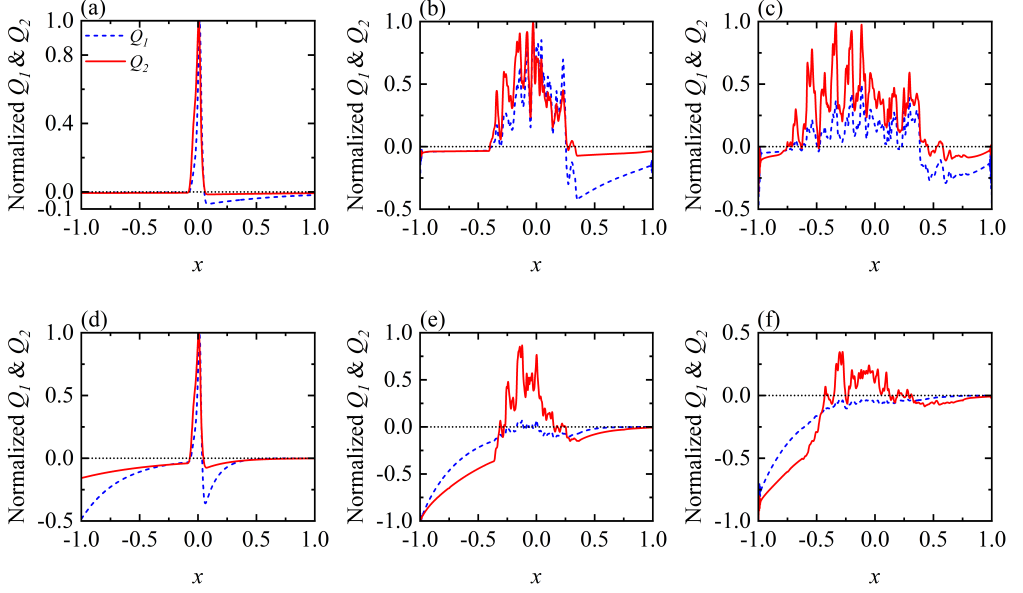


Figure 5: Identification of unstable regions based on the local instability criteria for incompressible flow  $Q_1 = -\frac{\partial \bar{p}}{\partial x} \frac{\partial \bar{p}}{\partial x}$ , and for compressible flow  $Q_2 = \bar{c}^2 \frac{\partial \bar{p}}{\partial x} - \frac{\partial \bar{p}}{\partial x}$ . The  $Q_2$  is equivalent to the expression (2.18) for the RT cases considered here, owing to the negative pressure gradient in gravitational field. The ordinate has been normalized by their maximum amplitudes. Subfigures (a)~(c) and (d)~(f) correspond to moments of  $t/\tau = 1, 2.5$  and  $4$  for the case of  $S_r = 0.5$  and  $3$  respectively.

Average the equation (2.19) to give:

$$\bar{p} = \overline{(\Gamma - 1)\rho e}. \quad (2.20)$$

With the Reynolds decomposition, the instantaneous variables  $p, \rho, \Gamma,$  and  $e$  can be written as  $p = \bar{p} + p', \rho = \bar{\rho} + \rho', \Gamma = \bar{\Gamma} + \Gamma',$  and  $e = \bar{e} + e',$  which are substituted into the equations (2.19) and (2.20), then subtracting equation (2.20) from equation (2.19) to yield the linear relation between fluctuation variables as follows

$$\rho' = \frac{\bar{\rho}}{\bar{p}} p' - \frac{\bar{\rho}}{\bar{e}} e' - \frac{\bar{\rho}}{\bar{\Gamma} - 1} \Gamma', \quad (2.21)$$

where the nonlinear fluctuation correlations are discarded. The adiabatic index fluctuation  $\Gamma'$  can be considered neglected due to the following reasons. Firstly, for mixtures comprising gases with identical molecular structures, the adiabatic index  $\Gamma_L$  and  $\Gamma_H$  of the light and heavy fluids are identical. Consequently,  $\Gamma$  of the mixture is independent of the species and can be treated as a constant, with  $\Gamma'$  becoming appreciable only at extreme temperatures which is beyond the scope of the present study. Secondly, for mixtures consisting of gases with different molecular structures, the variation in  $\Gamma$  of the mixture remains insignificant, even if the adiabatic index  $\Gamma_L$  and  $\Gamma_H$  of the light and heavy fluids are different and the  $\Gamma$  of the mixture is species-dependent. This is attributed to the small difference in adiabatic indices for gases with different molecular structures. For example,  $\Gamma = 1.4$  for diatomic gas,  $\Gamma = 1.33$  for polyatomic gas, it indicates negligible spatial gradients along the direction of mixing development. In contrast, the fluctuations in density, pressure, and internal energy are substantially larger than  $\Gamma',$  and as thus, the  $\Gamma'$  can be considered negligible. Consequently,

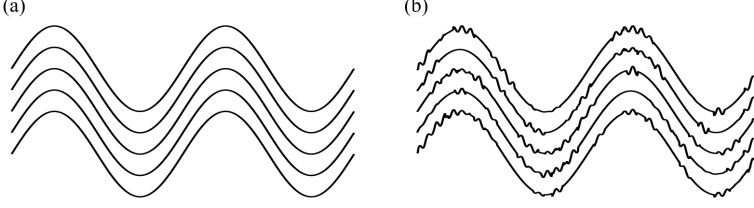


Figure 6: Schematic diagrams of two adjacent equilibrium states. The subfigure (a) gives the state A, a smooth ensemble average state; the subfigure (b) gives the state B, an instantaneous state evolving from the state A under small perturbations.

the equation (2.21) reduces to:

$$\rho' = \frac{\bar{\rho}}{\bar{p}} p' - \frac{\bar{\rho}}{\bar{e}} e'. \quad (2.22)$$

The mass flux velocity is then obtained by multiplying the equation (2.22) by  $u'$  and then applying averaging:

$$\overline{u_i''} = -\frac{\overline{\rho' u_i'}}{\bar{\rho}} = -\frac{\overline{p' u_i'}}{\bar{p}} + \frac{\overline{e' u_i'}}{\bar{e}}. \quad (2.23)$$

The local instability criterion (2.18) for compressible flows provides valuable insights for identifying unstable regions, offering critical inspiration for the development of a compressible RANS mixing model. This criterion is incorporated into the modeling of the mass flux velocity by combining with the thermodynamic Gibbs relation (Chassaing *et al.* (2002), chapter 6):

$$T \delta s = \delta h - \delta p / \rho, \quad (2.24)$$

where  $s$  denotes entropy. This relation is applied to the following scenario. Consider two adjacent equilibrium states, A and B, as illustrated in figure 6. Here, state A represents a smooth ensemble average state, while state B evolves from state A under small perturbations, corresponding to an instantaneous state. These perturbations are sufficiently small to satisfy the mathematical definition of variation, enabling a continuous transition from state A to state B. Consequently, the variations  $\delta s$ ,  $\delta h$ , and  $\delta p$  can be equated to the corresponding small perturbations  $s'$ ,  $h'$  and  $p'$  respectively, yielding:

$$T s' = h' - p' / \rho. \quad (2.25)$$

Substitute  $T = \bar{T} + T'$  and  $\rho = \bar{\rho} + \rho'$  into the equation (2.25) to yield the linear relation between fluctuation variables as follows

$$\bar{T} s' = h' - p' / \bar{\rho}, \quad (2.26)$$

where the nonlinear fluctuation correlations are discarded.

Next, substituting the pressure fluctuation in equation (2.23) with (2.26) yields:

$$\overline{u_i''} = -\frac{\overline{\rho' u_i'}}{\bar{\rho}} = -\frac{\bar{\rho}}{\bar{p}} \overline{h' u_i'} - \bar{T} s' u_i' + \frac{\overline{e' u_i'}}{\bar{e}} \approx \frac{\bar{\rho} \bar{T}}{\bar{p}} \overline{s' u_i'} - \frac{\bar{\rho}}{\bar{p}} \overline{e' u_i'}, \quad (2.27)$$

where  $h = \Gamma e$  is used, and the approximation arises from neglecting a third-order fluctuation correlation term and a  $\Gamma'$  term. These two terms in (2.27) will be modeled respectively.

Using the relation  $s = c_v \ln \frac{p}{\rho^\Gamma}$ ,  $\frac{\bar{\rho}\bar{T}}{\bar{p}} s' u'_i$  can be expressed as

$$\frac{\bar{\rho}\bar{T}}{\bar{p}} s' u'_i \approx \frac{\bar{\rho}\bar{T}\bar{c}_v}{\bar{p}} \left( \ln \frac{p}{\rho^\Gamma} \right)' u'_i, \quad (2.28)$$

where the fluctuations involving  $c'_v$  are ignored, similar to the treatment of Génin & Menon (2010). The expression (2.28) can be written as

$$\frac{\bar{\rho}\bar{T}\bar{c}_v}{\bar{p}} \left( \ln \frac{p}{\rho^\Gamma} \right)' u'_i = \frac{\bar{\rho}\bar{T}\bar{c}_v}{\bar{p}} \overline{(lnp - \Gamma ln\rho)' u'_i} \approx \frac{\bar{\rho}\bar{T}\bar{c}_v}{\bar{p}} \overline{(lnp)' u'_i - \bar{\Gamma} \overline{(ln\rho)' u'_i}}, \quad (2.29)$$

Where the term involving  $\Gamma'$  is ignored, as discussed earlier. The  $(lnp)'$  and  $(ln\rho)'$  are the fluctuation parts of  $lnp$  and  $ln\rho$  respectively, and can be obtained based on the following operation. Implement Taylor expansions for  $lnp$  and  $ln\rho$  surrounding with the mean parts  $\bar{p}$  and  $\bar{\rho}$ , reading  $lnp = \ln(\bar{p} + p') \approx \ln\bar{p} + p'/\bar{p} + O(p'^2)$ , and  $ln\rho = \ln(\bar{\rho} + \rho') \approx \ln\bar{\rho} + \rho'/\bar{\rho} + O(\rho'^2)$ , thus yielding  $(lnp)' \approx p'/\bar{p}$  and  $(ln\rho)' \approx \rho'/\bar{\rho}$  by discarding the nonlinear fluctuation correlations. Consequently, the expression (2.29) is transformed as

$$\frac{\bar{\rho}\bar{T}\bar{c}_v}{\bar{p}} \overline{(lnp)' u'_i - \bar{\Gamma} \overline{(ln\rho)' u'_i}} = \frac{\bar{\rho}\bar{T}\bar{c}_v}{\bar{p}} \overline{p' u'_i / \bar{p} - \bar{\Gamma} \rho' u'_i / \bar{\rho}}. \quad (2.30)$$

Based on the GDA, the (2.30) can be closed with the mean variables, i.e.

$$\frac{\bar{\rho}\bar{T}\bar{c}_v}{\bar{p}} \overline{p' u'_i / \bar{p} - \bar{\Gamma} \rho' u'_i / \bar{\rho}} = C_3 \nu_t \frac{\bar{\rho}\bar{T}\bar{c}_v}{\bar{p}} \left( -\frac{1}{\bar{p}} \frac{\partial \bar{p}}{\partial x_i} + \frac{\bar{\Gamma}}{\bar{\rho}} \frac{\partial \bar{\rho}}{\partial x_i} \right) = C_3 \nu_t \frac{\bar{\Gamma}}{\bar{\rho}(\bar{\Gamma} - 1)} \left( \frac{\partial \bar{p}}{\partial x_i} - \frac{1}{\bar{c}^2} \frac{\partial \bar{p}}{\partial x_i} \right), \quad (2.31)$$

where  $C_3$  is a model coefficient to be determined. It is evident that the closure in (2.31) is intrinsically linked to the compressibility criterion (2.18), highlighting the physical consistency of the proposed formulation.

Using the relation  $e = c_v T$ ,  $-\frac{\bar{\rho}}{\bar{p}} e' u'_i$  can be expressed as

$$-\frac{\bar{\rho}}{\bar{p}} e' u'_i \approx -\frac{\bar{\rho}\bar{c}_v}{\bar{p}} \overline{T' u'_i}, \quad (2.32)$$

where  $c'_v$  is ignored, similar to the treatment of (2.28). The pure turbulent heat flux  $\overline{T' u'_i}$  in (2.32) is straightforward modeled based on the expression proposed by Cloutman (2003), reading

$$\overline{T' u'_i} = -C_4 \nu_t \left( \frac{\partial \bar{T}}{\partial x_i} - \frac{\bar{\Gamma} - 1}{\bar{\Gamma}} \frac{\bar{T}}{\bar{p}} \frac{\partial \bar{p}}{\partial x_i} \right), \quad (2.33)$$

where  $C_4$  is a model coefficients to be determined. By combining with the (2.33), the  $-\frac{\bar{\rho}\bar{c}_v}{\bar{p}} \overline{T' u'_i}$  is expressed as

$$-\frac{\bar{\rho}\bar{c}_v}{\bar{p}} \overline{T' u'_i} = C_4 \nu_t \frac{\bar{c}_p}{\bar{\rho}\bar{c}^2} \left( \bar{\rho} \frac{\partial \bar{T}}{\partial x_i} - \frac{1}{\bar{c}_p} \frac{\partial \bar{p}}{\partial x_i} \right). \quad (2.34)$$

It is worth emphasizing that this formulation of (2.33) deviates from the conventional GDA framework by explicitly accounting for counter-gradient heat transport mechanisms. Classical gradient diffusion theories, such as Fourier's law, posit that heat transfer occurs from high-temperature to low-temperature regions, with flux magnitude proportional to the local temperature gradient. However, turbulent flow dynamics can induce anomalous heat

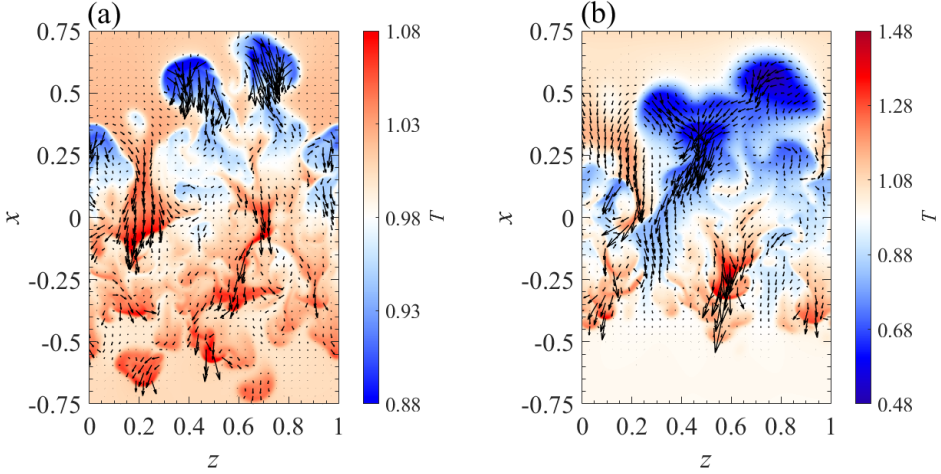


Figure 7: Contours of instantaneous temperature in the central  $x - z$  plane for cases of (a)  $S_r = 0.5$  and (b) 3 at  $t/\tau = 4$ . The instantaneous turbulent heat flux is also displayed with the vector arrows.

transport phenomena where heat is transferred against the temperature gradient—from low-temperature to high-temperature regions. Such a counter-gradient behavior is ubiquitously observed in convection-dominated boundary layer, buoyancy-dominated turbulence, turbulent coherent structures, among other scenarios.

In the density-stratified compressible RT mixing flows investigated in this study, counter-gradient heat transfer is observed, as clearly evidenced by the flow field visualization in figure 7. To elucidate this phenomenon, we analyze the late-stage flow field at  $t/\tau = 4$  from the central  $x - z$  plane of the 3D HiFi simulations for weak ( $S_r = 0.5$ ) and strong ( $S_r = 3$ ) stratification cases. The visualization employs a background temperature color map overlaid with instantaneous turbulent heat flux vectors  $\overline{T'u'_i}$ . Figure 7 reveals the following points. Firstly, the heavy fluid regions generally exhibit lower temperatures compared to the light fluid regions, and moreover, density stratification promotes a wider range of temperature variations across the mixing zone. Secondly, strong density stratification ( $S_r = 3$ ) contributes to produce organized large-scale flow structures, enhancing heat transfer efficiency. The case with weak density stratification ( $S_r = 0.5$ ) displays dispersed small-scale turbulent structures, resulting in heat transfer dominated by local mixing. Last but not least, the turbulent heat flux shows significant deviation from the local temperature gradient direction, with clear evidence of heat transfer from low-temperature to high-temperature regions. These findings underscore the importance of turbulent heat flux in the flows considered here, and further necessitate explicit consideration of counter-gradient diffusion in modeling  $\overline{T'u'_i}$ . Consequently, based on the work of Cloutman (2003), we adopt the closure formulation (2.33) to address the specific requirements of modeling counter-gradient diffusion in density-stratified compressible RT flows.

Finally, collecting the expressions (2.34) and (2.31), the turbulent mass flux velocity is modeled as

$$-\frac{\overline{\rho'u'_i}}{\bar{\rho}} = C_3 v_t \frac{\bar{\Gamma}}{\bar{\rho}(\bar{\Gamma} - 1)} \left( \frac{\partial \bar{\rho}}{\partial x_i} - \frac{1}{\bar{c}^2} \frac{\partial \bar{p}}{\partial x_i} \right) + C_4 v_t \frac{\bar{c}_p}{\bar{\rho} \bar{c}^2} \left( \bar{\rho} \frac{\partial \bar{T}}{\partial x_i} - \frac{1}{\bar{c}_p} \frac{\partial \bar{p}}{\partial x_i} \right). \quad (2.35)$$

Based on a principle of minimal modifications to the baseline model, the expression (2.35) is integrated into the baseline closure (2.12) for the local Atwood number  $A_{ssi}$ , yielding:

$$A_{ssi} = \frac{\tilde{L}}{\bar{\rho} + \tilde{L} \left| \frac{\partial \bar{\rho}}{\partial x_i} \right|} \left\{ C_3 \left[ \frac{\bar{\Gamma}}{\bar{\Gamma} - 1} \left( \frac{\partial \bar{\rho}}{\partial x_i} - \frac{1}{\bar{c}^2} \frac{\partial \bar{p}}{\partial x_i} \right) \right] + C_4 \frac{1}{\bar{c}^2} \left( \bar{\rho} \bar{c}_p \frac{\partial \bar{T}}{\partial x_i} - \frac{\partial \bar{p}}{\partial x_i} \right) \right\}. \quad (2.36)$$

To ensure consistency with the baseline form (2.12) in the incompressible limit  $\bar{c} \rightarrow \infty$ , the model coefficient  $C_3$  is required to meet the constraint

$$C_3 = \frac{C_A(\bar{\Gamma} - 1)}{\bar{\Gamma}}. \quad (2.37)$$

Additionally, it is found that the present model can achieve optimal predictions when  $C_4 = C_3$ , based on calibrations with HiFi data. Consequently,  $C_4 = C_3 = \frac{C_A(\bar{\Gamma} - 1)}{\bar{\Gamma}}$  is adopted in this study.

Finally, the local Atwood number  $A_{ssi}$  is expressed as

$$A_{ssi} = \frac{\tilde{L}}{\bar{\rho} + \tilde{L} \left| \frac{\partial \bar{\rho}}{\partial x_i} \right|} \left[ C_A \frac{\partial \bar{\rho}}{\partial x_i} + \underbrace{\frac{C_A(\bar{\Gamma} - 1)}{\bar{\Gamma}} \frac{1}{\bar{c}^2} \left( \bar{\rho} \bar{c}_p \frac{\partial \bar{T}}{\partial x_i} - \frac{2\bar{\Gamma} - 1}{\bar{\Gamma} - 1} \frac{\partial \bar{p}}{\partial x_i} \right)}_{\text{compressibility corrections}} \right]. \quad (2.38)$$

The second term in the expression (2.38) incorporates all compressibility corrections proposed here. Remarkably, this formulation maintains the original model coefficient  $C_A$  without introducing additional parameters, thereby preserving the simplicity of this model. In the incompressible limit  $c \rightarrow 0$ , the expression (2.38) naturally converges to its incompressible counterpart given by the formula (2.12), demonstrating consistency with the baseline formulation.

The proposed modeling strategy reveals that influences of the turbulent mass flux on evolution of compressible mixing flows predominantly stem from two key factors: turbulent entropy flux and turbulent heat flux. The present scheme physically captures density variations induced by both entropy and temperature fluctuations. From a perspective of RANS modeling, the proposed closure takes into accounts for two essential aspects of compressible mixing flows. Firstly, the conventional density gradient in the baseline model is replaced by the more physically representative entropy gradient. Secondly, turbulent heat effects are explicitly incorporated through a modified temperature gradient diffusion formulation that accounts for counter-gradient diffusion effect. These modeling considerations are expected to provide a comprehensive framework for capturing compressibility effects in variable-density compressible turbulent mixing flows.

### 3. Model validation

To evaluate the proposed compressibility corrections, density-stratified compressible RT mixing flows with different stratification parameters  $S_r$  are tested. The flow configurations, including model coefficients and initialization of turbulence model variables, remain consistent with the baseline model, as stated in section 2.2.

Figure 8 illustrates the temporal evolutions of bubble ( $W_b$ ) and spike ( $W_s$ ) mixing widths for 4 cases with density stratification parameters  $S_r$  ranging from 0.5 to 3. The proposed compressibility modifications show remarkable consistency with HiFi simulation results across all tested cases. This improved performance stems from two fundamental physical

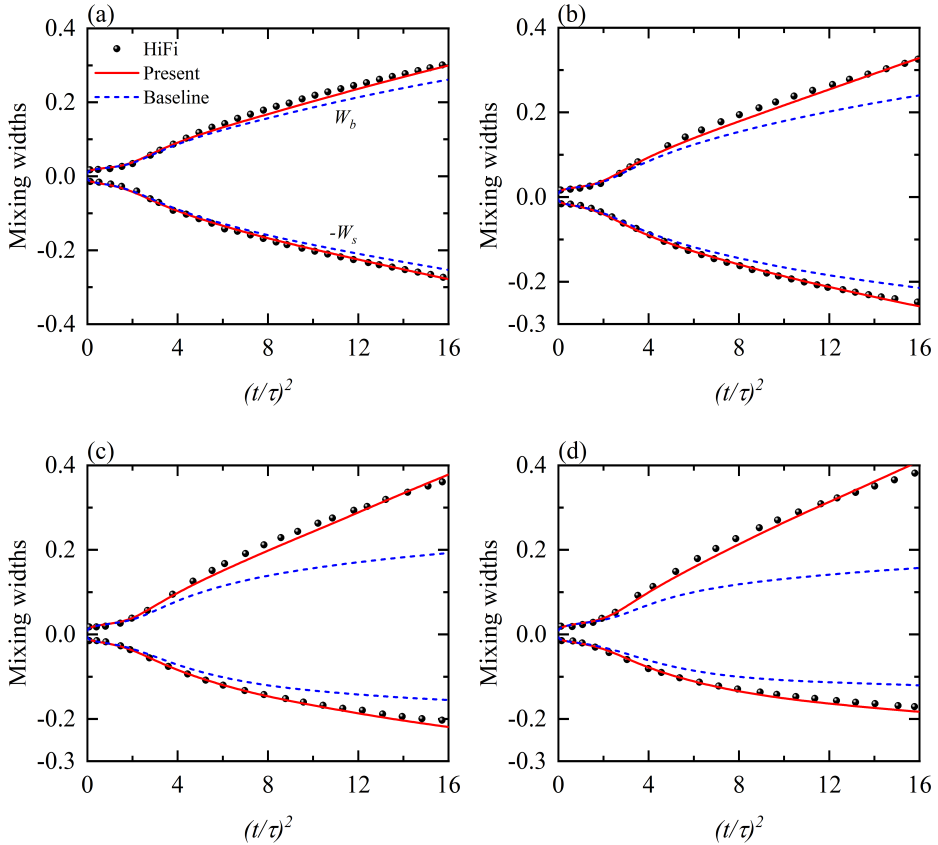


Figure 8: Temporal evolutions of the mixing widths. Subfigures (a) to (d) correspond to the cases of  $S_r = 0.5, 1, 2,$  and  $3,$  respectively.

considerations: incorporation of the local instability criterion for compressible flows, and appropriate treatment of turbulent heat flux contributions. By incorporating these effects, the model achieves a more comprehensive representation of the turbulence production term in the TKE equation, leading to significantly improved predictions of compressible mixing evolution. It should be noted that identical initialization of the turbulent model variables and model coefficients are maintained throughout all the cases. The model's robustness is particularly evident in strongly stratified cases ( $S_r=3$ ), where it still delivers accurate predictions despite the significant compressibility effect. The success of the compressible closure (2.38) without additional empirical coefficients stems from its physically grounded formulation, which effectively captures the essential dynamics of compressible mixing flows.

Except the temporal evolution of mixing width, spatial profiles of the important variables are also examined. Figure 9 presents the mass fraction profiles at three different moments  $t/\tau = 1, t/\tau = 2.5,$  and  $t/\tau = 4,$  across stratification parameters  $S_r$  varying from 0.5 to 3. Excellent agreements with HiFi simulations are observed for all cases, demonstrating the model's robust predictive capability. This validation is further reinforced by the density profile comparisons, as shown in figure 10, which serve as a critical metric for compressible flow characterization.

The density profile variations depicted in figure 10 show critical physical insights, offering a more direct understanding of the baseline model's distinct performance across cases with

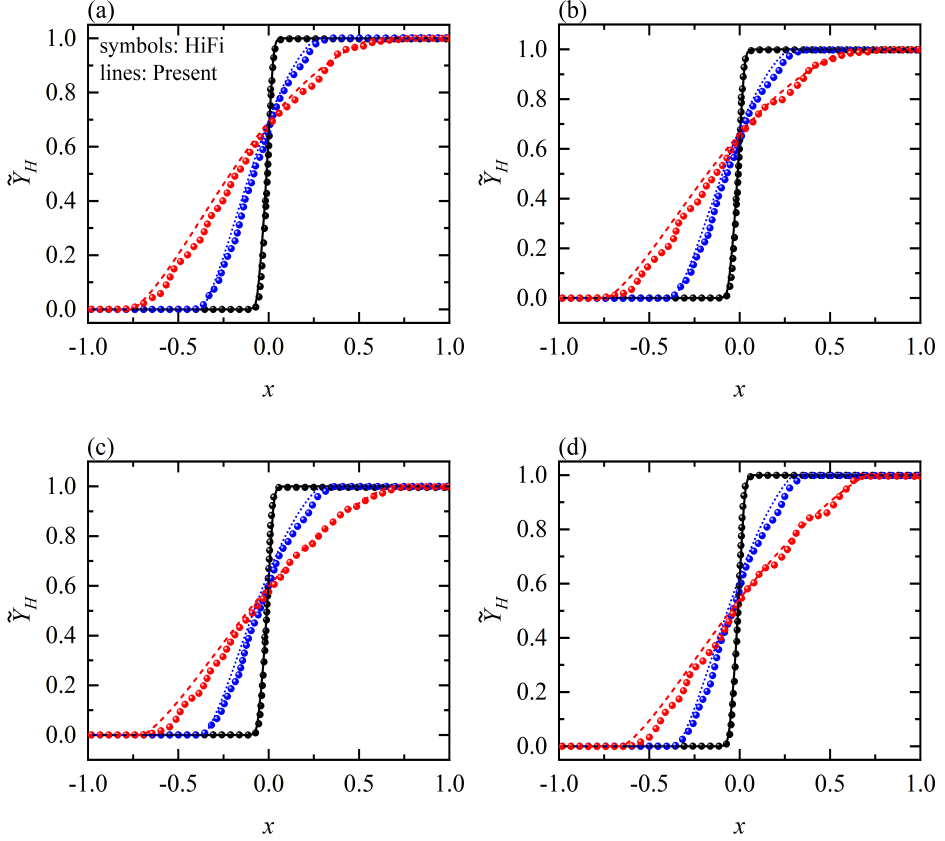


Figure 9: Spatial profiles of the mean species at three different moments  $t/\tau = 1$  (colored by black),  $t/\tau = 2.5$  (colored by blue), and  $t/\tau = 4$  (colored by red). Subfigures (a) to (d) correspond to the cases with  $S_r = 0.5, 1, 2,$  and  $3$ , respectively.

different  $S_r$ . Specifically, for the cases with a relatively small  $S_r$ , i.e.  $S_r = 0.5$  and  $1$ , the sustained positive density gradient throughout the simulation ensures an effective baroclinic production term. It leads to the baseline model's better performance for mixing width in cases with weaker stratification ( $S_r = 0.5$  and  $1$ ) compared to stronger stratification cases ( $S_r = 2$  and  $3$ ), as shown in figure 8. Additionally, it is also noted that compared to the case of  $S_r = 1$ , the baseline model shows superior accuracy for the case of  $S_r = 0.5$ , as the positive density gradient persists across the entire mixing region, providing a relatively sufficient TKE production term. However, for the case of  $S_r = 1$ , the positive density gradients become confined to the core mixing region at later stages, while negative gradients emerge at the edge of the mixing region. It is well-established that the amplitude of the mixing width depends on the penetration dynamics of bubbles and spikes at the edge of the mixing zone. In RANS simulation, the strength of penetration is closely linked to the amplitude of the TKE production term. Due to the disappearance of the baroclinic term at the edge (where the density gradient becomes negative), the TKE production term diminishes to zero, significantly reducing the TKE and halting further development of the mixing evolution. Consequently, the mixing width predicted by the baseline model is substantially lower than the actual physical evolution.

The underestimate of the mixing width for cases of  $S_r = 2$  and  $3$  can also be explained

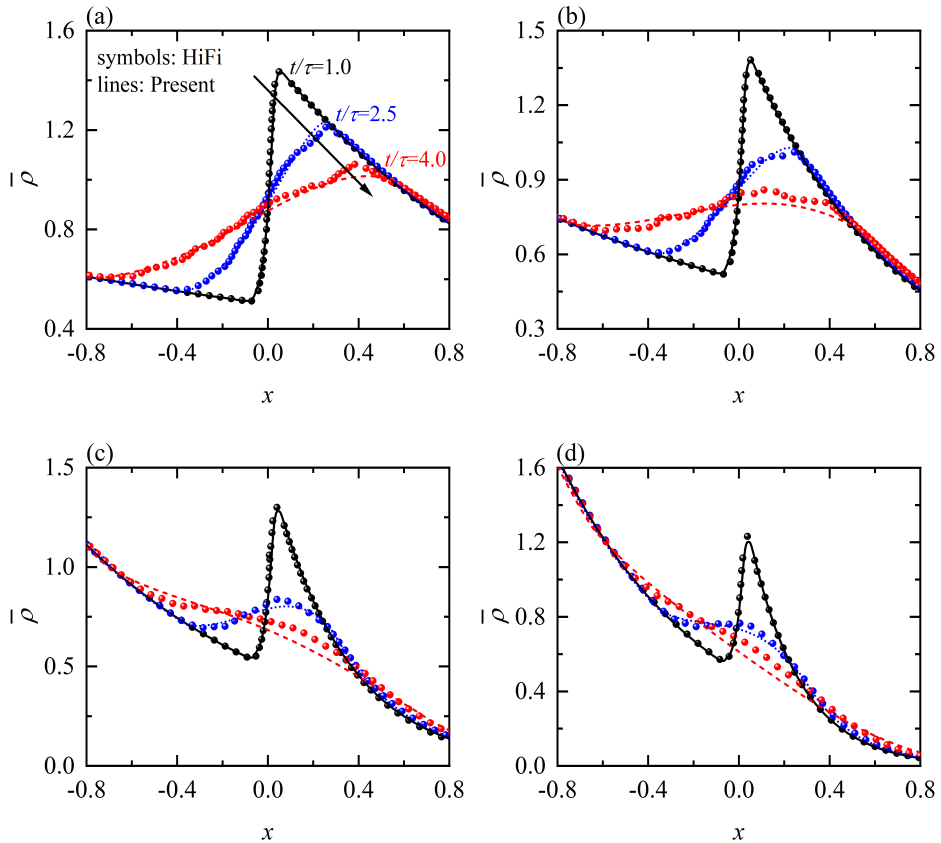


Figure 10: Spatial profiles of the mean density at three different moments  $t/\tau = 1$  (colored by black),  $t/\tau = 2.5$  (colored by blue), and  $t/\tau = 4$  (colored by red). Subfigures (a) to (d) correspond to the cases with  $S_r = 0.5, 1, 2,$  and  $3$ , respectively.

by the aforementioned analysis. For these cases, which exhibit strong density stratification, fundamentally different behavior is observed. The density gradient prematurely reverses sign during the simulation—occurring at the edge of the mixing region in the intermediate stage for  $S_r=2$  and across the entire mixing region in the intermediate stage for  $S_r=3$ . This gradient reversal causes a severe deficit in the turbulence production source. Since the baseline model’s closure relies solely on the baroclinic term, it fails to provide sufficient TKE production, leading to a deterioration in model performance with increasing stratification strength.

Section 2.2 establishes that flow regions where baroclinic terms vanish may maintain instability, as determined by the local instability criterion for compressible flows. This phenomenon has also been validated by HiFi simulations (Gauthier 2017; Luo & Wang 2022), which demonstrate ongoing mixing and turbulence development in density-stratified compressible RT flows despite baroclinic term disappearance. The proposed model incorporates more comprehensive physical mechanisms for compressible mixing flows and supplements the TKE production source appropriately, leading to successful predictions across all investigated cases.

#### 4. Summary and discussion

Compressible mixing flow induced by hydromechanics interfacial instability play a crucial role in engineering applications, such as the ICF. RANS simulations remain the most practical approach for engineering predictions. However, most of the existing RANS mixing models focus on the incompressible cases, and fail to predict compressible mixing flows accurately. This study examines the density-stratified RT flows as representative cases to: (i) identify limitations in the existing models for compressible flow predictions, and (ii) develop an improved compressible RANS mixing model. Our analysis begins with a comparative study of local instability criteria for incompressible versus compressible flows, demonstrating the physical inadequacy of conventional baroclinic term modeling ( $\frac{\partial \bar{p}}{\partial x_i} \frac{\partial \bar{p}}{\partial x_i}$ ) for compressible cases. Subsequently, based on the  $K - L - \gamma$  mixing transition model proposed by Xie *et al.* (2025), we derive compressibility corrections for modeling the key turbulent mass flux term in the TKE equation. Validation studies across various density-stratified compressible RT cases confirm the model's improved predictive capability. Compared with the incompressible baseline model, two fundamental improvements account for the proposed model's success. One is incorporation of the local instability criterion for compressible flows, and the other is proper consideration of turbulent heat flux effect, which prove significant in flows considered here. Moreover, the proposed modifications maintain simplicity without introducing additional model coefficient, while substantially enhancing its accuracy for compressible mixing flows.

While elements of the proposed modeling formulation have appeared in previous studies, their application to RANS modeling of interfacial mixing flows remains limited. The present closure shares some similar modeling with formulations dating back nearly four decades in stellar evolution studies (Cloutman 1987). Furthermore, the kinetic closure model for turbulent counter-gradient diffusion developed by Cloutman (2003) provides theoretical support for modeling the turbulent heat flux in this study. In the existing studies, several researchers have employed partial versions of the current compressibility corrections. For instance, the  $K - \epsilon$  model by Morán-López & Schilling (2013) use a similar form  $\frac{\partial \bar{p}}{\partial x_i} - \frac{\bar{\rho}}{\bar{p}} \frac{\partial \bar{p}}{\partial x_i}$  to close the turbulent mass flux velocity  $\overline{u_i''}$ . Zhou (2017b) have similarly emphasized the importance of entropy gradients in modeling the TKE equation's buoyancy source term. However, these pioneering contributions have received relatively little attention in modeling interfacial mixing flows. This may be attributed to the predominantly incompressible or weakly compressible nature of previously studied flows, where compressibility effects are insufficiently pronounced to demonstrate the models' full potential.

Contributions of this study include the following points. Firstly, we present a systematic derivation of comprehensive compressibility closures based on the EOS of perfect gas and the thermodynamics law. This represents a significant advance over previous sporadic and incomplete formulations found in the literature. The developed closures maintain both physical fidelity and computational tractability. Second, our results demonstrate the crucial role of turbulent heat flux in compressible flows, while it is ignored in incompressible cases. Through detailed analysis, it is revealed that turbulent heat flux: (i) significantly modifies buoyancy effects by mediating density fluctuations, and (ii) exhibits counter-gradient diffusion behavior in density-stratified compressible RT flows. The latter has not been uncovered in the existing reports, to our knowledge. It necessitate specific modifications, while the traditional GDA fails to describe that. Thirdly, this work provides the first successful RANS-based framework for predicting density-stratified compressible RT flows, representing a significant step forward in turbulence modeling for practical engineering applications.

While the proposed model shows promising results in the density-stratified compressible

RT mixing flows, its performance for the compressible RM and KH mixing problems remains to be verified in the future. The present study primarily establishes a foundational modeling strategy for compressible mixing flows, with comprehensive verification left for future investigation.

#### Acknowledgements.

This work was supported by the National Natural Science Foundation of China (Grant Nos. 12222203, 92152202, and 12432010) and the National Key Laboratory of Computational Physics (Grant No. 6142A05240201). Additionally, Luo, T. was supported by the Research Grants Council (RGC) of the Hong Kong Special Administrative Region, China (Project Reference: AoE/P-601/23-N) and the Center for Ocean Research in Hong Kong and Macau (CORE), a joint research center between the Laoshan Laboratory and the Hong Kong University of Science and Technology (HKUST).

#### Declaration of Interests.

The authors report no conflict of interest.

### REFERENCES

- CHANDRASEKHAR, S. 1961 *Hydrodynamic and hydromagnetic stability*. Oxford-Clarendon Press and New York-Oxford Univ. Press.
- CHASSAING, P., ANTONIA, R., ANSELMET, F., JOLY, L. & SARKAR, S. 2002 *Variable Density Fluid Turbulence*. Springer Netherlands: Imprint: Springer.
- CLOUTMAN, L. D. 1987 A new estimate of the mixing length and convective overshooting in massive stars. *Astrophys. J.* **313**, 699–710.
- CLOUTMAN, L. D. 2003 Compressibility corrections to closure approximations for turbulent flow simulations. *Tech. Rep.*. Lawrence Livermore National Lab. (LLNL), Livermore, CA (United States).
- CRAXTON, R. S., ANDERSON, K. S., BOEHLY, T. R., GONCHAROV, V. N., HARDING, D. R., KNAUER, J. P., MCCRORY, R. L., MCKENTY, P. W., MEYERHOFER, D. D., MYATT, J. F., SCHMITT, A. J., SETHIAN, J. D., SHORT, R. W., SKUPSKY, S., THEOBALD, W., KRUEER, W. L., TANAKA, K., BETTI, R., COLLINS, T. J. B., DELETTREZ, J. A., HU, S. X., MAROZAS, J. A., MAXIMOV, A. V., MICHEL, D. T., RADHA, P. B., REGAN, S. P., SANGSTER, T. C., SEKA, W., SOLODOV, A. A., SOURES, J. M., STOECKL, C. & ZUEGEL, J. D. 2015 Direct-drive inertial confinement fusion: A review. *Phys. Plasmas* **22** (11), 110501.
- DENISSEN, N., ROLLIN, B., REISNER, J. & ANDREWS, M. 2014 The tilted rocket rig: A Rayleigh-Taylor test case for RANS models. *J. Fluids Eng.* **136**, 091301.
- DIMONTE, G. & TIPTON, R. 2006 K-L turbulence model for the self-similar growth of the Rayleigh-Taylor and Richtmyer-Meshkov instabilities. *Phys. Fluids* **18** (8), 85101.
- FU, CHENQUAN, ZHAO, ZHIYE, XU, XIN, WANG, PEI, LIU, NANSHENG, WAN, ZHENHUA & LU, XIYUN 2022 Nonlinear saturation of bubble evolution in a two-dimensional single-mode stratified compressible Rayleigh-Taylor instability. *Phys. Rev. Fluids* **7**, 023902.
- GAMALII, E. G., ROZANOV, V. B., SAMARSKII, A. A., TISHKIN, V. F., TYURINA, N. N. & FAVORSKII, A. P. 1980 Hydrodynamic stability of compression of spherical laser targets. *Sov. Phys. JETP* **52**, 230–237.
- GAUTHIER, S. 2013 Compressibility effects in Rayleigh-Taylor flows: influence of the stratification. *Phys. Scr.* **2013** (T155), 014012.
- GAUTHIER, SERGE 2017 Compressible Rayleigh-Taylor turbulent mixing layer between newtonian miscible fluids. *J. Fluid Mech.* **830**, 211–256.
- GAUTHIER, S. & LE CREURER, B. 2010 Compressibility effects in Rayleigh-Taylor instability-induced flows. *Philos. T. R. Soc. A* **368** (1916), 1681–1704.
- GÉNIN, F. & MENON, S. 2010 Simulation of turbulent mixing behind a strut injector in supersonic flow. *AIAA J.* **48** (3), 526–539.
- GEORGE, E. & GLIMM, J. 2005 Self-similarity of Rayleigh-Taylor mixing rates. *Phys. Fluids* **17** (5), 054101.
- HELMHOLTZ, V. 1868 On discontinuous movements of fluids. *Lond. Edinb. Dubl. Phil. Mag. J. Sci.* **36** (244), 337–346.
- JIN, H., LIU, X. F., LU, T., CHENG, B., GLIMM, J. & SHARP, D. H. 2005 Rayleigh-Taylor mixing rates for compressible flow. *Phys. Fluids* **17** (2), 024104.

- KELVIN, L. 1871 Hydrokinetic solutions and observations. *Lond. Edinb. Dubl. Phil. Mag. J. Sci.* **42** (281), 362–377.
- KOKKINAKIS, I. W., DRIKAKIS, D. & YOUNGS, D. L. 2019 Modeling of Rayleigh-Taylor mixing using single-fluid models. *Phys. Rev. E* **99**, 013104.
- KOKKINAKIS, I. W., DRIKAKIS, D. & YOUNGS, D. L. 2020 Two-equation and multi-fluid turbulence models for Richtmyer-Meshkov mixing. *Phys. Fluids* **32** (7), 074102.
- KOKKINAKIS, I. W., DRIKAKIS, D., YOUNGS, D. L. & WILLIAMS, R. J. R. 2015 Two-equation and multi fluid turbulence models for Rayleigh-Taylor mixing. *Int. J. Heat Fluid Fl.* **56**, 233–250.
- LI, HAIFENG, HE, ZHIWEI, ZHANG, YOUSHENG & TIAN, BAOLIN 2019 On the role of rarefaction/compression waves in Richtmyer-Meshkov instability with reshock. *Phys. Fluids* **31** (5), 054102.
- LIVESCU, D. 2004 Compressibility effects on the Rayleigh-Taylor instability growth between immiscible fluids. *Phys. Fluids* **16** (1), 118–127.
- LIVESCU, D. 2013 Numerical simulations of two-fluid turbulent mixing at large density ratios and applications to the Rayleigh-Taylor instability. *Philos. Trans. R. Soc. A* **371** (2013), 20120185.
- LUO, TENGFEI, LI, ZHIJIE, YUAN, ZELONG, PENG, WENHUI, LIU, TIANYUAN, WANG, LIANGZHU (LEON) & WANG, JIANCHUN 2024 Fourier neural operator for large eddy simulation of compressible Rayleigh-Taylor turbulence. *Phys. Fluids* **36** (7), 075165.
- LUO, TENGFEI & WANG, JIANCHUN 2022 Mixing and energy transfer in compressible Rayleigh-Taylor turbulence for initial isothermal stratification. *Phys. Rev. Fluids* **7**, 104608.
- MESHKOV, E. E. 1969 Instability of the interface of two gases accelerated by a shock wave. *Fluid Dyn.* **4** (5), 101–104.
- MORÁN-LÓPEZ, J. & SCHILLING, O. 2013 Multicomponent Reynolds-averaged Navier-Stokes simulations of reshocked Richtmyer-Meshkov instability-induced mixing. *High Energy Density Phys.* **9**, 112–121.
- MORGAN, B. & GREENOUGH, J. 2015 Large-eddy and unsteady RANS simulations of a shock-accelerated heavy gas cylinder. *Shock Waves* **26**.
- QI, HAN, HE, ZHI-WEI, XU, AI-GUO & ZHANG, YOU-SHENG 2024 The vortex structure and enstrophy of the mixing transition induced by Rayleigh-Taylor instability. *Phys. Fluids* **36** (11), 114107.
- RAYLEIGH, L. 1882 Investigation of the Character of the Equilibrium of an Incompressible Heavy Fluid of Variable Density. *Proc. Lond. Math. Soc.* **201** (1), 170–177.
- RICHTMYER, R. D. 1960 Taylor instability in shock acceleration of compressible fluids. *Commun. Pure Appl. Math.* **13** (2), 297–319.
- TAYLOR, G. 1950 The Instability of Liquid Surfaces when Accelerated in a Direction Perpendicular to their Planes. I. *Proc. R. Soc. Lond., Ser. A* **201** (1065), 192.
- THORNBER, B., DRIKAKIS, D., WILLIAMS, R. J. R. & YOUNGS, D. 2008a On entropy generation and dissipation of kinetic energy in high-resolution shock-capturing schemes. *J. Comput. Phys.* **227** (10), 4853–4872.
- THORNBER, B., MOSEDALE, A., DRIKAKIS, D., YOUNGS, D. & WILLIAMS, R. J. R. 2008b An improved reconstruction method for compressible flows with low mach number features. *J. Comput. Phys.* **227** (10), 4873–4894.
- TORO, E. F., SPRUCE, M. & SPEARES, W. 1994 Restoration of the contact surface in the HLL-Riemann solver. *Shock Waves* **4**, 25–34.
- XIAO, M., HU, Z., DAI, Z. & ZHANG, Y. 2022 Experimentally consistent large-eddy simulation of re-shocked Richtmyer-Meshkov turbulent mixing. *Phys. Fluids* **34** (12), 125125.
- XIAO, MENGJUAN, QI, HAN & ZHANG, YOUSHENG 2025 Local transition indicator and modelling of turbulent mixing based on the mixing state. *J. Fluid Mech.* **1002**, A4.
- XIAO, M., ZHANG, Y. & TIAN, B. 2020 Modeling of turbulent mixing with an improved K-L model. *Phys. Fluids* **32** (9), 092104.
- XIE, HANSONG, QI, HAN, XIAO, MENGJUAN, ZHANG, YOUSHENG & ZHAO, YAOMIN 2025 An intermittency based Reynolds-averaged transition model for mixing flows induced by interfacial instabilities. *J. Fluid Mech.* **1002**, A31.
- XIE, H., ZHAO, Y. & ZHANG, Y. 2023 Data-driven nonlinear K-L turbulent mixing model via gene expression programming method. *Acta Mech. Sin.* **39** (2), 322315.
- XIE, HAN-SONG, XIAO, MENG-JUAN & ZHANG, YOU-SHENG 2021a Predicting different turbulent mixing problems with the same  $k-\epsilon$  model and model coefficients. *AIP Advances* **11** (7), 075213.
- XIE, H.-S., XIAO, M.-J. & ZHANG, Y.-S. 2021b Unified prediction of turbulent mixing induced by interfacial instabilities via Besnard-Harlow-Rauenzahn-2 model. *Phys. Fluids* **33** (10), 105123.
- XUE, CHUANG & YE, WENHUA 2010 Destabilizing effect of compressibility on Rayleigh-Taylor instability for fluids with fixed density profile. *Phys. Plasmas* **17** (4), 042705.

- ZHANG, Y., HE, Z., XIE, H., XIAO, M. & TIAN, B. 2020 Methodology for determining coefficients of turbulent mixing model. *J. Fluid Mech.* **905**, A26.
- ZHAO, D., BETTI, R. & ALUIE, H. 2022 Scale interactions and anisotropy in Rayleigh-Taylor turbulence. *J. Fluid Mech.* **930**, A29.
- ZHAO, ZHIYE, LIU, NANSHENG & LU, XIYUN 2020 Kinetic energy and enstrophy transfer in compressible Rayleigh-Taylor turbulence. *J. Fluid Mech.* **904**, A37.
- ZHOU, Y. 2017a Rayleigh-Taylor and Richtmyer-Meshkov instability induced flow, turbulence, and mixing. I. *Phys. Rep.* **720-722**, 1–136.
- ZHOU, Y. 2017b Rayleigh-Taylor and Richtmyer-Meshkov instability induced flow, turbulence, and mixing. II. *Phys. Rep.* **723-725**, 1–160.